

Visualizing Deep Convolutional Neural Networks Using Natural Pre-Images

Aravindh Mahendran^{*} and Andrea Vedaldi[†]

University of Oxford

July 17, 2022

Abstract

Image representations, from SIFT and bag of visual words to Convolutional Neural Networks (CNNs), are a crucial component of almost all computer vision systems. However, our understanding of them remains limited. In this paper we study several landmark representations, both shallow and deep, by a number of complementary visualization techniques. These visualizations are based on the concept of “natural pre-image”, namely a naturally-looking image whose representation has some notable property. We study in particular three such visualizations: inversion, in which the aim is to reconstruct an image from its representation, activation maximization, in which we search for patterns that maximally stimulate a representation component, and caricaturization, in which the visual patterns that a representation detects in an image are exaggerated. We pose this as a regularized energy-minimization framework and demonstrate its generality and effectiveness. In particular, we show that this method can invert representations such as HOG more accurately than recent alternatives while being applicable to CNNs too. Among our findings, we show that several layers in CNNs retain photographically accurate information about the image, with different degrees of geometric and photometric invariance.

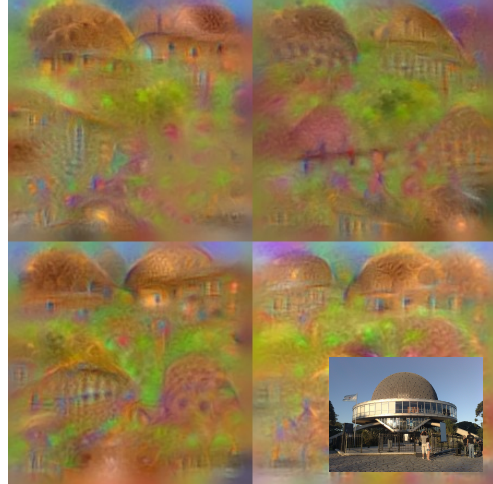


Figure 1: Four reconstructions of the bottom-right image obtained from the 1,000 code extracted from the last fully connected layer of the VGG-M CNN [2]. This figure is best viewed in color.

1 Introduction

Most image understanding and computer vision methods do not operate directly on images, but on suitable image representations. Notable examples of representations include textons [22], histogram of oriented gradients (SIFT [25] and HOG [5]), bag of visual words [4][36], sparse [46] and local coding [43], super vector coding [51], VLAD [15], Fisher Vectors [31], and, lately,

^{*}aravindh@robots.ox.ac.uk

[†]vedaldi@robots.ox.ac.uk

deep neural networks, particularly of the convolutional variety [20, 34, 49]. While the performance of representations has been improving significantly in the past few years, their design remains eminently empirical. This is true for shallower hand-crafted features such as HOG or SIFT and even more so for the latest generation of deep representations, such as deep Convolutional Neural Networks (CNNs), where millions of parameters are learned from data. A consequence of this complexity is that our understanding of such representations is limited.

Aiming at obtaining a better understanding of representations, in this paper we develop a family of methods to investigate CNNs and other image features by means of visualizations. All these methods are based on the common idea of seeking natural-looking images that representations are notable in some useful sense. We call these *natural pre-images* and propose a unified formulation and algorithm to compute them (section 3).

Within this framework, we explore three particular types of visualizations. In the first type, called **inversion** (section 5), we compute the “inverse” of a representation (Figure 1). We do so by modelling a representation as a function $\Phi_0 = \Phi(\mathbf{x}_0)$ of the image \mathbf{x}_0 . Then, we attempt to recover the image from the information contained only in the code Φ_0 . Notably, most representations Φ are *not* invertible functions; for example, a representation that is *invariant* to nuisance factors such as viewpoint and illumination removes this information from the image. Our aim is to characterize this loss of information by studying the equivalence class of images \mathbf{x}^* that share the same representation $\Phi(\mathbf{x}^*) = \Phi_0$.

In **activation maximization** (section 6), the second visualization type, we look instead for an image \mathbf{x}^* that maximally excites a certain component $[\Phi(\mathbf{x})]_i$ of the representation. The resulting image is representative of the visual stimuli that are selected by that component and helps understanding its “meaning” or function. This type of visualization is sometimes referred to as “deep dream” as it can be interpreted as the result of the representation “imagining” a concept.

In our third and last visualization type, which we call **caricaturization** (section 7), we modify an initial image \mathbf{x}_0 to exaggerate any pattern that excites the representation $\Phi(\mathbf{x}_0)$. Differently from activation maximization, this visualization emphasizes the meaning of combinations of representation components that are active to-

gether.

Several of these ideas have been explored by us and others in prior work as detailed in section 2. In particular, the idea of visualizing representations using pre-images has been explored in connection with neural networks since at least the work of Linden *et al.* [23].

Our first contribution is to introduce the idea of a *natural pre-image* [27], i.e. to restrict reconstructions to the set of natural images. While this is difficult to achieve in practice, we explore different regularization methods (section 3.2) that can work as a proxy, including regularizers using the Total Variation (TV) norm of the image. We also explore indirect regularization methods such as applying random jitters to the reconstruction as suggested by Mordvintsev *et al.* [28].

Our second contribution is to consolidate different visualization and representation types, including inversion, activation maximization, and caricaturization, in a common framework (section 3). We propose a single algorithm applicable to a large variety of representations, from SIFT to very deep CNNs, using essentially a single set of parameters. The algorithm is based on optimizing an energy function using gradient descent and back-propagation through the representation architecture.

Our third contribution is to use these techniques to apply the three visualization types to the study of several different representations. First, we show that, despite its simplicity and generality, our method recovers significantly better reconstructions for shallow representations such as HOG compared to recent alternatives [42] (section 5.1). In order to do so, we also rebuild the HOG and DSIFT representations as equivalent CNNs, simplifying the computation of their derivatives as required by our algorithm (4.1). Second, we apply inversion (section 5.2), activation maximization (section 6), and caricaturization (section 7) to the study of CNNs, treating each layer of a CNN as a different representations, and studying different state-of-the-art architectures, from AlexNet, to VGG-M, and VGG very deep (section 4.2). As we do so, we emphasize a number of general properties of such representations, as well as differences between them. In particular, we study the effect of depth on representations, showing that CNNs gradually build an increasing amount of invariance and complexity, layer after layer.

Our findings are summarized in section 8. The code for the experiments in this paper and extended visualiza-

tions are available at <http://www.robots.ox.ac.uk/~vgg/research/invrep/index.html>. This code uses the open-source MatConvNet toolbox [41] and publicly-available copies of the models to allow to easy reproduction of the results.

This paper is a substantially extended version of [27], which introduced the idea of natural pre-image, but was limited to visualizations by inversion.

2 Related work

With the development of modern visual representations, there has been an increasing interest in developing visualization methods to understand them. Most of the recent contributions [28, 47] build on the idea of *natural* pre-images introduced in [27], extending or applying it in different ways. In turn, this work is based on several prior contributions that have used pre-images to understand neural networks and classical computer vision representations such as HOG and SIFT. The rest of the section discusses these relationships in detail.

2.1 Natural pre-images

Mahendran *et al.* [27] note that not all pre-images are equally interesting in visualization; instead, more meaningful results can be obtained by restricting pre-images to the set of natural images. This particularly true in the study of discriminative models such as CNNs that are essentially “unspecified” outside the domain of natural images used to train them. While capturing the concept of natural image in an algorithm is difficult in practice, the authors of [27] proposed to use simple natural image priors as a proxy, and formulated that in a regularized energy minimization framework. Among these, the the most important regularizer was the TV norm of the reconstructed image (section 3.2).

The visual quality of pre-images can be further improved by introducing complementary regularization methods. Google’s “inceptionism” [28], for example, contributed the idea of regularization through jittering. They shift the pre-image randomly during optimization, resulting in sharper and more vivid reconstructions. The work of Yosinski *et al.* [47] used yet another regularizer. They applied Gaussian blurring and clipped pixels, that

have small values or that have a small effect on activating components in a CNN representation, to zero.

2.2 Methods for finding pre-images

The use of pre-images to visualize representations has a long history. Simonyan *et al.* [35] applied this idea to recent CNNs and optimized, starting from random noise and by means of back-propagation and gradient descent, the response of individual filters in the last layer of a deep convolutional neural network – an example of activation maximization. Related energy-minimization frameworks were adopted by [27, 28, 47] to visualize modern CNNs. Prior to that, very similar methods were applied to early neural networks in [21, 23, 26, 45], using gradient descent or optimization strategies based on sampling.

Several pre-image methods alternative to energy minimization have been explored as well. Nguyen *et al.* [29] use genetic programming to generate images that maximize the response of selected neurons in the very last layer of a modern CNN, corresponding to an image classifier. Vondrick *et al.* [42] learn a regressor that, given a HOG-encoded image patch, reconstructs the input image. Weinzaepfel *et al.* [44] reconstruct an image from SIFT features using a large vocabulary of patches to invert individual detections and then blend the results using Laplace (harmonic) interpolation. Earlier works [16, 39] specialized on inverting networks in the context of dynamical systems and will not be discussed further here.

The DeConvNet method of Zeiler and Fergus [49] “transposes” CNNs to find which image patches are responsible for certain neural activations. While transposition operation applied to CNNs is somewhat heuristic, Simonyan *et al.* [35] showed that it approximates the derivative of the CNN and that, therefore, DeConvNet is analogous to one step of the backpropagation algorithm used in their energy minimization framework. A significant difference, however, is that in DeConvNet the authors transfer the pattern of activations of max-pooling layers from the direct CNN evaluation to the transposed one, therefore copying rather than inferring this geometric information during reconstruction.

A related line of work [1, 7] is to learn a second neural network to act as the inverse of the original one, but this is complicated by the fact that the inverse is usually not unique. Therefore, these methods may regress an “aver-

age pre-image” conditioned on the target representation, which may not be as effective as sampling the pre-image if the goal is to characterize representation ambiguities. A benefit is that these methods can be significantly faster than energy minimization.

Finally, the vast family of auto-encoder architectures [14] train networks together with their inverses as a form of auto-supervision; here we are interested instead in visualizing feed-forward and discriminatively-trained CNNs now popular in computer vision.

2.3 Types of visualizations using pre-images

Pre-images can be used to generate a large variety of complementary visualizations, many of which have been applied before to a variety of representations.

The idea of **inverting representations** in order to recover an image from its encoding was used to study SIFT in the work of [44], Local Binary Descriptors by d’Angelo *et al.* [6], HOG in [42] and bag of visual words descriptors in Kato *et al.* [18]. In [27] we looked at the inversion problem for HOG, SIFT, and modern CNNs; our method differs significantly from the ones above as it addresses many different representations using the same energy minimization framework and optimization algorithm. Compared to existing inversion techniques for dense shallow representations such as HOG [42], it is also shown to achieve superior results, both quantitatively and qualitatively.

Perhaps the first to apply **activation maximization** to recent CNNs such as AlexNet [20] is the work of Simonyan *et al.* [35], where this technique was used to maximize the response of neural activations in the last layer of a deep CNN. Since these responses are learned to correspond to specific object classes, this produces versions of the object as conceptualized by the CNN, sometimes called “deep dreams”. Recently, Google has generated similar visualizations for their inception network [28] and Yosinski *et al.* [47] have applied activation maximization to the visualizations not only to the last layers of a CNN, but also to intermediate representation components. Related extensive component-specific visualizations were conducted in [49], albeit in their DeConvNet framework. The idea dates back in fact to at least [9], which introduced activation maximization to visualize deep networks learned from the MNIST digit dataset.

A first version of **caricaturization** was explored in [35] to maximize image features corresponding to a particular object class, although this was ultimately used to generate saliency maps rather than to generate an image. Google [28] explored extensively caricaturization in their “inceptionism” research with two remarkable results. The first one was to show which visual structures are captured at different levels in a deep CNN. The second one was to show that CNNs can be used to generate aesthetically pleasing images.

In addition to these three broad visualization categories, there are several others which are more specific. In DeConvNet [49], for example, visualizations are obtained by activation maximization, but the starting point is not a random image, but an image, searched in a large dataset, that causes a given representation component to strongly activate. The network is then evaluated feed-forward and the location of the max-pooling activations is recorded. Combined with the transpose “deconvolutional network”, this information is used to generate crisp visualizations of the most excited neural paths. However, this differs from both inversion and activation maximization in that it does make use of information beyond the one contained in the representation output itself.

2.4 Activation statistics

Inversion, activation maximization, and caricaturization help understanding the nature of representations by looking at which visual patterns excite certain representation components. Alternatively, it is possible to investigate the information captured in activation statistics. This idea traces back to the seminal work of Portilla and Simoncelli [32] in modelling textures. Recently, the same principles have been applied to modern CNN by Gatys *et al.* [12], looking in particular at the information contained in the empirical correlation between feature channels in the convolutional layers of CNNs. They showed that such statistics provide good models of visual textures, better than the ones that were obtained from wavelets in [32].

In [11] the same authors apply the idea not to inversion, but to caricaturization by modifying a given image in order to match the empirical correlation of deep features measured from another image. In this manner, they show that the artistic style of particular painter can be transferred from an image to another.

2.5 Fooling representations

A line of research related to visualization by pre-images is the one that looks at “fooling representations”. Here the goal is to generate images that a representations assign to particular categories despite having a distinctly incompatible semantics. Some of these methods looking for *adversarial perturbations* of a source image. For instance, Tatu *et al.* [38] show that it is possible to make any two images look nearly identical in SIFT space up to the injection of adversarial noise in the data. The complementary effect was demonstrated for CNNs by Szegedy *et al.* [37], where an imperceptible amount of adversarial noise was shown to change the predicted class of an image to any desired class. The latter observation was confirmed and extended by [29]. The instability of representations appear in contradiction with results in [27, 42, 44] that show that HOG, SIFT, and early layers of CNNs are largely invertible. This apparent inconsistency could be resolved by noting that [29, 37, 38] require the injection of adversarial noise which is very unlikely to occur in natural images. It is not unlikely that enforcing representation to be sufficiently regular, e.g. Lipschitz continuous, would avoid the issue.

The work by [29] proposes a second method to generate confounders. In this case, they use genetic programming to create, using a sequence of editing operations, an image that is classified as any desired class by the CNN, while looking nothing like an instance of that class. While the CNN does not have a background class that could be used to reject such images, the result is remarkable.

3 A method for finding the pre-images of a representation

This section introduces our method to find pre-images of an image representation. This method will then be applied to the inversion, activation maximization, and caricaturization problems. These are formulated as regularized energy minimization problems where the goal is to find a natural-looking image whose representation has a desired property [45]. Formally, given a representation function $\Phi : \mathbb{R}^{H \times W \times D} \rightarrow \mathbb{R}^d$ and a reference code $\Phi_0 \in \mathbb{R}^d$, we

seek for the image¹ $\mathbf{x} \in \mathbb{R}^{H \times W \times D}$ that minimizes the objective function:

$$\mathbf{x}^* = \underset{\mathbf{x} \in \mathbb{R}^{H \times W \times D}}{\operatorname{argmin}} \mathcal{R}_\alpha(\mathbf{x}) + \mathcal{R}_{TV^\beta}(\mathbf{x}) + C\ell(\Phi(\mathbf{x}), \Phi_0) \quad (1)$$

The loss ℓ compares the image representation $\Phi(\mathbf{x})$ to the target value Φ_0 , the two regularizer terms $\mathcal{R}_\alpha + \mathcal{R}_{TV^\beta} : \mathbb{R}^{H \times W \times D} \rightarrow \mathbb{R}_+$ capture a *natural image prior*, and the constant C trades-off loss and regularizers. The latter are designed to be roughly balanced, such that $C = 1$ is often a reasonable value for this parameter. The meaning of minimizing the objective function (1) depends on the choice of the loss and of the regularizer terms as discussed in the following sections.

3.1 Loss functions

Choosing different loss functions ℓ in Equation 7 results in different visualizations. In *inversion*, ℓ is set to the Euclidean distance:

$$\ell(\Phi(\mathbf{x}), \Phi_0) = \frac{\|\Phi(\mathbf{x}) - \Phi_0\|^2}{\|\Phi_0\|^2}, \quad (2)$$

where $\Phi_0 = \Phi(\mathbf{x}_0)$ is the representation of a target image. Minimizing (1) results in an image \mathbf{x}^* that “resembles” \mathbf{x}_0 from the viewpoint of the representation.

Sometimes it is interesting to restrict the reconstruction to a subset of the representation components. This is done by introducing a binary *mask* M of the same dimension of Φ_0 and by modifying Equation 2 as follows:

$$\ell(\Phi(\mathbf{x}), \Phi_0; M) = \frac{\|(\Phi(\mathbf{x}) - \Phi_0) \odot M\|^2}{\|\Phi_0 \odot M\|^2}, \quad (3)$$

In *activation maximization* and *caricaturization*, $\Phi_0 \in \mathbb{R}_+^d$ is treated instead as a weight vector selecting which representation components should be maximally activated. This is obtained by considering the inner product:

$$\ell(\Phi(\mathbf{x}), \Phi_0) = -\frac{1}{Z} \langle \Phi(\mathbf{x}), \Phi_0 \rangle. \quad (4)$$

For example, if $\Phi_0 = \mathbf{e}_i$ is the indicator vector of the i -th component of the representation, minimizing Equation 4

¹In the following, the image \mathbf{x} is assumed to have null mean, as required by most CNN implementations.

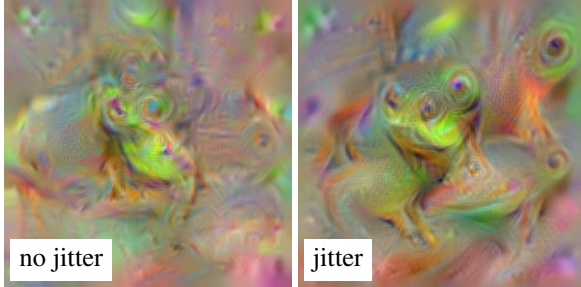


Figure 3: Effect of the jitter regularizer in activation maximization for the “tree frog” neuron in the fc8 layer in AlexNet. Jitter helps recovering larger and crispier image structures.

maximizes the component $[\Phi(\mathbf{x})]_i$. Alternatively, if Φ_0 is set to $\max\{\Phi(\mathbf{x}_0), 0\}$, the minimization of Equation 1 will highlight components that are strongly active in the representation $\Phi(\mathbf{x}_0)$ of a reference image \mathbf{x}_0 , while ignoring the inactive components.

The choice of the normalization constant Z in activation maximization and caricaturization will be discussed later. Note also that, for the loss Equation 4, there is no need to define a separate mask as this can be pre-multiplied into Φ_0 .

3.2 Regularization

Discriminative representations discard a significant amount of low-level image information that is irrelevant to the target task (e.g. image classification). As this information is nonetheless useful for visualization, we propose to partially recover it by restricting the inversion to the subset of natural images $\mathcal{X} \subset \mathbb{R}^{H \times W \times D}$. This is motivated by the fact that, since representations are applied to natural images, there is comparatively little interest in understanding their behavior outside of this set. However, modeling the set of natural images is a significant challenge in its own right. As a proxy, we propose to regularize the reconstruction by using simple *image priors* implemented as regularizers in Equation 1. We experiment in particular with three such regularizers, discussed next.

3.2.1 Bounded range

The first regularizer encourages the intensity of pixels to stay bounded. This is important for networks that include normalization layers, as in this case rescaling the image range has no effect on the network output. In activation maximisation, it is even more important for networks that do *not* include normalization layers, as in this case increasing the image range increases neural activations by the same amount.

In [27] this regularizer was implemented as a soft constraint using the penalty $\|\mathbf{x}\|_\alpha^\alpha$ for a large value of the exponent α . Here we modify it in several ways. First, for color images we make the term isotropic in RGB space by considering the norm

$$N_\alpha(\mathbf{x}) = \frac{1}{HWB^\alpha} \sum_{v=1}^H \sum_{u=1}^W \left(\sum_{k=1}^D \mathbf{x}(v, u, k)^2 \right)^{\frac{\alpha}{2}} \quad (5)$$

where v indexes the image rows, u the image columns, and k the color channels. By comparison, the norm used in [27] is non-isotropic and might slightly bias the reconstruction of the colors.

The term is normalized by the image area HW and by the scalar B . This scalar is set to the typical L^2 norm of the pixel RGB vector, such that $N_\alpha(\mathbf{x}) \approx 1$.

The soft constraint $N_\alpha(\mathbf{x})$ is combined with a hard constraint to limit the pixel intensity to be at most B_+ :

$$R_\alpha(\mathbf{x}) = \begin{cases} N_\alpha(\mathbf{x}), & \forall v, u : \sqrt{\sum_k \mathbf{x}(v, u, k)^2} \leq B_+ \\ +\infty, & \text{otherwise.} \end{cases} \quad (6)$$

While the hard constraint may seem sufficient, in practice it was observed that without soft constraints pixels tend to saturate in the reconstructions.

3.2.2 Bounded variation

The second regularizer is the *total variation* (TV) $\mathcal{R}_{TV^\beta}(\mathbf{x})$ of the image, encouraging reconstructions to consist of piece-wise constant patches. For a discrete image \mathbf{x} , the TV norm is approximated using finite differ-

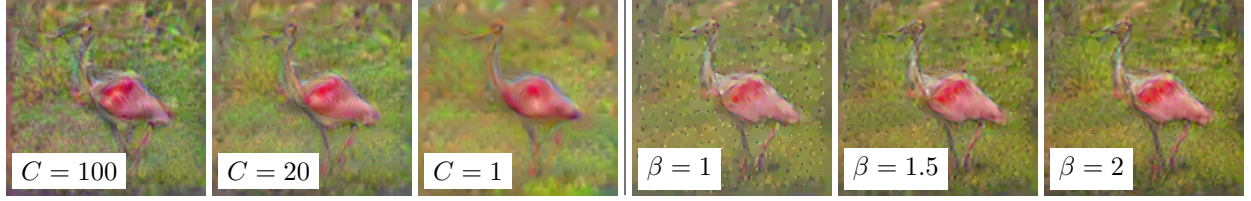


Figure 2: *Left*: Effect of the data term strength C in inverting a deep representation (the relu3 layer in AlexNet). Selecting a small value of C results in more regularized reconstructions, which is essential to obtain good results. *Right*: Effect of the TV regularizer β exponent; note the spikes for $\beta = 1$.

ences as follows:

$$\mathcal{R}_{TV^\beta}(\mathbf{x}) = \frac{1}{HWV^\beta} \sum_{uvk} \left((\mathbf{x}(v, u+1, k) - \mathbf{x}(v, u, k))^2 + (\mathbf{x}(v+1, u, k) - \mathbf{x}(v, u, k))^2 \right)^{\frac{\beta}{2}}.$$

where $\beta = 1$. Here the constant V in the normalization coefficient is the typical value of the norm of the gradient in the image.

The standard TV regularizer, obtained for $\beta = 1$, was observed to introduce unwanted ‘‘spikes’’ in the reconstruction, as illustrated in Figure 2 (right) when inverting a layer of a CNN. This is a known problem in TV-based image interpolation (see *e.g.* Figure 3 in [3]); the ‘‘spikes’’ occur at the locations of the samples because: (1) the TV norm along any path between two samples depends only on the overall amount of intensity change (not on the sharpness of the changes) and (2) integrated on the 2D image, it is optimal to concentrate sharp changes around a boundary with a small perimeter. Hyper-Laplacian priors with $\beta < 1$ are often used as a better match of the gradient statistics of natural images [19], but they only exacerbate this issue. Instead, we trade-off the sharpness of the image with the removal of such artifacts by choosing $\beta > 1$ which, by penalizing large gradients, distributes changes across regions rather than concentrating them at a point or a curve. We refer to this as the TV^β regularizer. As seen in Figure 2 (right), the spikes are removed for $\beta = 1.5, 2$ but the image is blurrier than for $\beta = 1$. At the same time, Figure 2 (left) illustrates the importance of using the TV regularizer in obtaining clean reconstructions.

3.2.3 Jitter

The last regularizer, which is inspired by [28], has an implicit form and consists in randomly shifting the input image before feeding it to the representation. Namely, we consider the optimization problem

$$\mathbf{x}^* = \underset{\mathbf{x} \in \mathbb{R}^{H \times W \times C}}{\operatorname{argmin}} E_\tau[\ell(\Phi(\operatorname{jitter}(\mathbf{x}; \tau)), \Phi_0)] + \lambda \mathcal{R}(\mathbf{x}) \quad (7)$$

where $E(\cdot)$ denotes expectation, $\tau \in [0, \dots, T-1]^2$ is a small random translation, and the $\operatorname{jitter}(\cdot)$ operator translates and crops \mathbf{x} :

$$[\operatorname{jitter}(\mathbf{x}; \tau)](v, u) = \mathbf{x}(v + \tau_2, u + \tau_1)$$

where $1 \leq v \leq H - T + 1$ and $1 \leq u \leq W - T + 1$. Jittering counterbalances the very significant downsampling performed by the earlier layers of deep CNNs, interpolating between pixels in back-propagation. This generally results in crispier pre-images, particularly in the activation maximization problem (Figure 3).

3.3 Balancing the loss and the regularizers

One difficulty in implementing a successful image reconstruction algorithm using the formulation of Equation 1 is to correctly balance the different terms. For this reason, the loss functions and regularizers are tuned in such a manner that, for reasonable reconstruction \mathbf{x} , they have comparable values (around unity). Unless otherwise noted, in the experiments we use the values, $C = 1$, $\alpha = 6$, $\beta = 2$, $B = 80$, $B_+ = 2B$, and $V = B/6.5$.

Algorithm 1 Stochastic gradient descent for pre-image

Require: Given the objective function $E(\cdot)$ and the learning rate η_0

- 1: $G_0 \leftarrow 0, \mu_0 \leftarrow 0$
- 2: Initialize \mathbf{x}_1 to random noise
- 3: **for** $t = 1$ to T **do**
- 4: $g_t \leftarrow \nabla E(\mathbf{x}_t)$ (using backprop)
- 5: $G_t \leftarrow \rho G_{t-1} + g_t^2$ (component-wise)
- 6: $\eta_t \leftarrow \frac{1}{\frac{1}{\eta_0} + \sqrt{G_t}}$ (component-wise)
- 7: $\mu_t \leftarrow \rho \mu_{t-1} - \eta_t g_t$
- 8: $\mathbf{x}_{t+1} \leftarrow \Pi_{B_+}(\mathbf{x}_t + \mu_t)$
- 9: **end for**

3.4 Optimization

Finding a minimizer of the objective (1) may seem difficult as most representations Φ are strongly non-linear; in particular, deep representations are a composition of several non-linear layers. Nevertheless, simple gradient descent (GD) procedures have been shown to be very effective in *learning* such models from data, which is arguably an even harder task. In practice, a variant of GD was found to result in good reconstructions.

The algorithm, whose pseudocode is given in Algorithm 1, is a variant of AdaGrad [8]. Like in AdaGrad, the algorithm automatically adapts the learning rate of individual components of the vector \mathbf{x}_t by scaling it by the inverse of the accumulated squared gradient G_t . Similarly to AdaDelta [48], however, it accumulates gradients only in a short temporal window, using the momentum coefficient $\rho = 0.9$. The gradient scaled by the adaptive learning rate $\eta_t g_t$ is accumulated to a momentum vector μ_t with the same factor ρ . The momentum is then summed to the current reconstruction \mathbf{x}_t and the result is projected back on the feasible region $[-B_+, B_+]$. Unless otherwise noted, the algorithm is run for $T = 300$ iterations, which was found to be a conservative choice.

While the learning rate η_t is adapted automatically during the optimization, at the first iteration $G_0 \approx 0$ and $\eta_1 = 1/(1/\eta_0 + \sqrt{G_0}) \approx \eta_0$. In practice, during the first several iterations the learning rate η_t is approximately equal to the *initial learning rate* η_0 . This learning rate is tuned based on the step size that would minimize the term $R_\alpha(\mathbf{x})$ in one iteration (ignoring momentum):

$0 \approx \mathbf{x}_2 = \mathbf{x}_1 - \bar{\eta}_0 \nabla R_\alpha(\mathbf{x}_1)$. Assuming that all pixels in \mathbf{x}_1 have intensity equal to the parameter B introduced above, then one obtains the condition $0 = B - \bar{\eta}_1 \alpha / B$ so that $\bar{\eta}_1 = B^2 / \alpha$. The initial learning rate η_0 is set as a fraction of this value:

$$\eta_1 = 0.01 \bar{\eta}_1 = 0.01 \frac{B^2}{\alpha}.$$

4 Representations

In this section, the image representations studied in the paper - dense SIFT, HOG, and several reference deep CNNs, are described. It is also shown how DSIFT and HOG can be implemented in a standard CNN framework, including computing their derivatives as required by the algorithms of section 3.4.

4.1 Classical representations

The *histograms of oriented gradients* are probably the best known family of “classical” computer vision features. Popularized by Lowe in [24] with the SIFT descriptor, here we consider two densely-sampled versions [30], namely DSIFT (Dense SIFT) and HOG [5]. In the remainder of this sub-section we describe in detail these two architectures as particular examples of CNNs. This clarifies the relationship between SIFT, HOG, and CNNs in general and allows implementing them in standard CNN toolboxes for experimentation. The DSIFT and HOG implementations in the VLFeat library [40] are used as numerical references. These are equivalent to Lowe’s [24] SIFT and the DPM V5 HOG [10, 13].

SIFT and HOG involve: computing and binning image gradients, pooling binned gradients into cell histograms, grouping cells into blocks, and normalizing the blocks. Denote by \mathbf{g} the image gradient at a given pixel and consider binning this into one of K orientations (where $K = 8$ for SIFT and $K = 18$ for HOG). This can be obtained in two steps: directional filtering and gating. The k^{th} directional filter is $G_k = u_{1k} G_x + u_{2k} G_y$ where

$$\mathbf{u}_k = \begin{bmatrix} \cos \frac{2\pi k}{K} \\ \sin \frac{2\pi k}{K} \end{bmatrix}, \quad G_x = \begin{bmatrix} 0 & 0 & 0 \\ -1 & 0 & 1 \\ 0 & 0 & 0 \end{bmatrix}, \quad G_y = G_x^\top.$$

layer name	0	1	2	3	4	5	6	7	8	9	10	11	12	13
n/a	n/a	conv1	relu1	norm1	pool1	conv2	relu2	norm2	pool2	conv3	relu3	conv4	relu4	conv5
ker. size	n/a	11	1	1	3	5	1	1	3	3	1	3	1	3
r.f. size	n/a	11	11	11	19	51	51	51	67	99	99	131	131	163
r.f. stride	n/a	4	4	4	8	8	8	8	16	16	16	16	16	16
dim.	3	96	96	96	96	256	256	256	256	384	384	384	384	256
layer name	14	15	16	17	18	19	20	21						
relu5	pool5	fc6	relu6	fc7	relu7	fc8	prob							
ker. size	1	3	6	1	1	1	1	1						
r.f. size	163	195	355	355	355	355	355	355						
r.f. stride	16	32	32	32	32	32	32	32						
dim.	256	256	4096	4096	4096	4096	1000	1000						

Table 1: **AlexNet structure.** The table lists the layers in AlexNet, their type, local receptive field size (ker.), the receptive field size in the input image (r. size), and number of feature channels (dim.). Note that, due to downsampling and padding, the receptive field size can be larger than the size of the input image (227×227).

layer name	0	1	2	3	4	5	6	7	8	9	10	11	12	13
n/a	n/a	conv1	relu1	norm1	pool1	conv2	relu2	norm2	pool2	conv3	relu3	conv4	relu4	conv5
ker. size	n/a	7	1	1	3	5	1	1	3	3	1	3	1	3
r.f. size	n/a	7	7	7	11	27	27	27	43	75	75	107	107	139
r.f. stride	n/a	2	2	2	4	8	8	8	16	16	16	16	16	16
dim.	3	96	96	96	96	256	256	256	256	512	512	512	512	512
layer name	14	15	16	17	18	19	20	21						
relu5	pool5	fc6	relu6	fc7	relu7	fc8	prob							
ker. size	1	3	6	1	1	1	1	1						
r.f. size	139	171	331	331	331	331	331	331						
r.f. stride	16	32	32	32	32	32	32	32						
dim.	512	512	4096	4096	4096	4096	1000	1000						

Table 2: **VGG-M structure.** The structure of the VGG-M neural network, similar to Table 1.

layer name	0	1	2	3	4	5	6	7	8	9	10	11	12	13
n/a	n/a	conv1'1	relu1'1	conv1'2	relu1'2	pool1	conv2'1	relu2'1	conv2'2	relu2'2	pool2	conv3'1	relu3'1	conv3'2
ker. size	n/a	3	1	3	1	2	3	1	3	1	2	3	1	3
r.f. field	n/a	3	3	5	5	6	10	10	14	14	16	24	24	32
r.f. stride	n/a	1	1	1	1	2	2	2	2	2	4	4	4	4
dim.	3	64	64	64	64	64	128	128	128	128	128	256	256	256
layer name	14	15	16	17	18	19	20	21	22	23	24	25	26	27
relu3'2	conv3'3	relu3'3	pool3	conv4'1	relu4'1	conv4'2	relu4'2	conv4'3	relu4'3	pool4	conv5'1	relu5'1	conv5'2	
ker. size	1	3	1	2	3	1	3	1	3	1	2	3	1	3
r.f. size	32	40	40	44	60	60	76	76	92	92	100	132	132	164
r.f. stride	4	4	4	8	8	8	8	8	8	8	16	16	16	16
dim.	256	256	256	256	512	512	512	512	512	512	512	512	512	512
layer name	28	29	30	31	32	33	34	35	36	37				
relu5'2	conv5'3	relu5'3	pool5	fc6	relu6	fc7	relu7	fc8	prob					
ker. size	1	3	1	2	7	1	1	1	1	1				
r.f. size	164	196	196	212	404	404	404	404	404	404				
r.f. stride	16	16	16	32	32	32	32	32	32	32				
dim.	512	512	512	512	4096	4096	4096	4096	1000	1000				

Table 3: **VGG-VD structure.** The structure of the VGG-VD-16 neural network, similar to Table 1.

The output of a directional filter is the projection $\langle \mathbf{g}, \mathbf{u}_k \rangle$ of the gradient along direction \mathbf{u}_k . A suitable gating function implements binning into a histogram element h_k . DSIFT uses bilinear orientation binning, given by

$$h_k = \|\mathbf{g}\| \max \left\{ 0, 1 - \frac{K}{2\pi} \cos^{-1} \frac{\langle \mathbf{g}, \mathbf{u}_k \rangle}{\|\mathbf{g}\|} \right\},$$

whereas HOG (in the DPM V5 variant) uses hard assignments $h_k = \|\mathbf{g}\| \mathbf{1}[\langle \mathbf{g}, \mathbf{u}_k \rangle > \|\mathbf{g}\| \cos \pi/K]$. Filtering is a standard CNN operation but these binning functions are not. While their implementation is simple, an interesting alternative is the approximated bilinear binning:

$$\begin{aligned} h_k &\approx \|\mathbf{g}\| \max \left\{ 0, \frac{1}{1-a} \frac{\langle \mathbf{g}, \mathbf{u}_k \rangle}{\|\mathbf{g}\|} - \frac{a}{1-a} \right\} \\ &\propto \max \{0, \langle \mathbf{g}, \mathbf{u}_k \rangle - a\|\mathbf{g}\| \}, \quad a = \cos 2\pi/K. \end{aligned}$$

The norm-dependent offset $\|\mathbf{g}\|$ is still non-standard, but the ReLU operator is, which shows to which extent approximate binning can be achieved in typical CNNs.

The next step is to pool the binned gradients into cell histograms using bilinear spatial pooling, followed by extracting blocks of 2×2 (HOG) or 4×4 (SIFT) cells. Both such operations can be implemented by banks of linear filters. Cell blocks are then l^2 normalised, which is a special case of the standard local response normalization layer. For HOG, blocks are further decomposed back into cells, which requires another filter bank. Finally, the descriptor values are clamped from above by applying $y = \min\{x, 0.2\}$ to each component, which can be reduced to a combination of linear and ReLU layers.

The conclusion is that approximations to DSIFT and HOG can be implemented with conventional CNN components plus the non-conventional gradient norm offset. However, all the filters involved are much sparser and simpler than the generic 3D filters in learned CNNs. Nonetheless, in the rest of the paper we will use exact CNN equivalents of DSIFT and HOG, using modified or additional CNN components as needed.² These CNNs

²This requires addressing a few more subtleties. In DSIFT gradient contributions are usually weighted by a Gaussian centered at each descriptor (a 4×4 cell block); here we use the VLFeat approximation (fast option) of weighting cells rather than gradients, which can be incorporated in the block-forming filters. In UoCTTI HOG, cells contain both oriented and unoriented gradients (27 components in total) as well as 4 texture components. The latter are ignored for simplicity, while the

are numerically indistinguishable from the VLFeat reference implementations, but, true to their CNN nature, allow computing the feature derivatives as required by the algorithm of section 3.

4.2 Deep convolutional neural networks

The first CNN model considered in this paper is **AlexNet**. Due to its popularity, we use the implementation that ships with the Caffe framework [17], which closely reproduces the original network by Krizhevsky *et al.* [20]. Occasionally, we also consider the **CaffeNet**, a network similar to AlexNet that also comes with Caffe. This and many other similar networks alternate the following computational building blocks: linear convolution, ReLU gating, spatial max-pooling, and local response normalization. Each such block takes as input a d -dimensional image and produces as output a k -dimensional one. Blocks can additionally pad the image (with zeros for the convolutional blocks and with $-\infty$ for max pooling) or sub-sample the data. The last several layers are deemed “fully connected” as the support of the linear filters coincides with the size of the image; however, they are equivalent to filtering layers in all other respects. Table 1 details the structure of AlexNet.

The second network is the **VGG-M** model from [2] (Table 2). VGG-M structure is very similar to AlexNet, with the following differences: it includes a significantly larger number of filters in the different layers, filters at the beginning of the network are smaller, and filter strides (subsampling) is reduced. While the network is slower than AlexNet, it also performs much better on the ImageNet ILSVRC 2012 data.

The last network is the **VGG-VD-16** model from [35] (Table 3). VGG-VD-16 is also similar to AlexNet, but with more substantial changes compared to VGG-M. Filters are very narrow (3×3) and very densely sampled. There are no normalization layers. Most importantly, the network contains many more intermediate convolutional

unoriented gradients are obtained as average of the oriented ones in the block-forming filters. Curiously, in UoCTTI HOG the l^2 normalization factor is computed considering only the unoriented gradient components in a block, but applied to all, which requires modifying the normalization operator. Finally, when blocks are decomposed back to cells, they are averaged rather than stacked as in the original Dalal-Triggs HOG, which can be implemented in the block-decomposition filters.

descriptors method	HOG HOGgle	HOG our	HOGb our	DSIFT our
error (%)	60.1 ± 11.6	36.6 ± 17.3	11.5 ± 4.8	9.4 ± 8.6

Table 4: Average reconstruction error of different representation inversion methods, applied to HOG and DSIFT. HOGb denotes HOG with bilinear orientation assignments. The standard deviation shown is the standard deviation of the error and not the standard deviation of the mean error.

layers. The resulting model is very slow, but very powerful; it won in fact a few competitions in the ImageNet ILSVRC 2014 challenge and has since become a standard model in the literature.

All pre-trained models are implemented in the MatConvNet framework and are publicly available at <http://www.vlfeat.org/matconvnet/pretrained>.

5 Visualization by inversion

The first set of experiments investigates visualizing representations using the inversion method. The objective function Equation 1 is setup to use the L^2 loss (section 3.1) to a target representation $\Phi_0 = \Phi(\mathbf{x}_0)$, where \mathbf{x}_0 is a sample image. Importantly, the optimization starts by initializing the reconstructed image \mathbf{x}_1 to random i.i.d. noise such that *the only information available to the algorithm is the code Φ_0* .

When initialized with different random seeds, this method should be expected to generate different reconstructions. This is because representations are invariant to nuisance and other factors and therefore do not have a unique pre-image. Instead, by observing the differences between reconstructed images it is possible to obtain insights on the nature of such invariances.

5.1 Inverting classical representations: SIFT and HOG

This section evaluates the representation inversion method of section 3 by applying it to HOG and DSIFT. The parameter C , trading off regularization and feature

reconstruction fidelity, is set the value 20 unless otherwise noted. Jitter is not used and the other parameters are set as stated in section 3.3. HOG and DSIFT cell sizes are set to 8 pixels.

The analysis includes both a qualitative (Figure 4) and quantitative (Table 4) comparison with existing techniques.

The quantitative evaluation reports a normalized reconstruction error $\|\Phi(\mathbf{x}^*) - \Phi(\mathbf{x}_i)\|_2 / \|\Phi(\mathbf{x}_i)\|_2$ averaged over images \mathbf{x}_i extracted from the first 100 ILSVRC 2012 challenge [33] validation images.

The closest alternative to our method is HOGgle, a technique introduced by Vondrick *et al.* [42] for the visualization of HOG features. The HOGgle code is publicly available from the authors’ website and is used throughout these experiments. Crucially, HOGgle is pre-trained to invert the UoCTTI implementation of HOG, which is numerically equivalent to CNN-HOG (section 4), allowing for a direct comparison between algorithms.

Compared to our method, HOGgle is fast (2-3s vs. 60s on the same CPU) but not very accurate, as it is apparent both qualitatively (Figure 4.c vs. d) and quantitatively (60.1% vs. 36.6% reconstruction error, see Table 4). Interestingly, [42] propose a direct optimization method similar to (1), but show that it does not perform better than HOGgle. This demonstrates the importance of the choice of regularizer and the ability of computing analytically the derivative of the representation in order to implement the optimization efficiently.

In terms of speed, an advantage of optimizing (1) is that it can be switched to use GPU code immediately given the underlying CNN framework; doing so results in a ten-fold speed-up. Furthermore the CNN-based implementations of HOG and DSIFT are currently unoptimized and it should be possible to accelerate them several times.

It is also apparent that different representations can be easier or harder to invert. In particular, modifying HOG to use bilinear gradient orientation assignments as SIFT (section 4) significantly reduces the reconstruction error (from 36.6% down to 11.5%) and improves the reconstruction quality (Figure 4.e). More impressive is DSIFT: it is quantitatively similar to HOG with bilinear orientation assignment, but produces significantly more detailed images (Figure 4.f). Since HOG uses a finer quantization of the gradient compared to SIFT but otherwise the same cell size and sampling, this result can be imputed

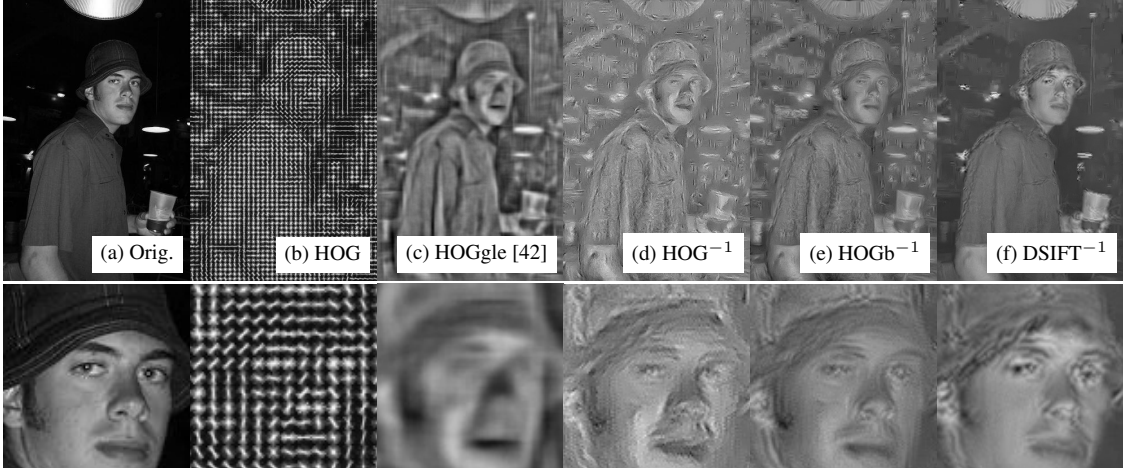


Figure 4: Reconstruction quality of different representation inversion methods, applied to HOG and DSIFT. HOGb denotes HOG with bilinear orientation assignments. This image is best viewed on screen.

to the heavier block-normalization of HOG that evidently discards more image information than SIFT.

5.2 Inverting CNNs

This section visualizes AlexNet, VGG-M, and VGG-VD-16 using the inversion method. The parameter C , trading off regularization and feature reconstruction fidelity, is set to one of $\{1, 20, 100, 300\}$, as indicated later. The jitter amount T is set to a quarter of the *stride* of the representation (after rounding); the stride is the step in the receptive field of representation components when stepping through spatial locations. Its value is given in Table 1-2-3. The other parameters are set as stated in section 3.3.

5.2.1 Reconstruction accuracy

Similar to section 5.1, the first experiment evaluates the ability of the algorithm to recover an image whose representation closely matches the target. As before, the algorithm is applied to 100 ImageNet ILSVRC validation images [20] (these images were not used to train the CNN). The experiment is repeated for all the layers of AlexNet and for different values of the parameter C to assess its effect. The resulting average normalized inversion errors are reported in Table 5.

CNNs such as Alex Net are significantly larger and deeper than the CNN implementation of HOG and DSIFT. It seems therefore that the inversion problem should be considerably harder in this case. Instead, the results of Table 5 compared to Table 4 indicate that CNNs are, in fact, not much more difficult to invert than HOG. In particular, the reconstruction error rarely exceeds 20%, which is comparable to the accuracy for HOG. The hardest layers to invert are the middle ones, while the last one achieves small reconstruction error of less than 10%. Therefore, the non-linearities in the CNN seem to be rather benign, which could explain why SGD can learn these models successfully.

Choosing a large regularization factor (small C) significantly deteriorates the quality of the reconstruction of the earlier layers of the network. At the same time, larger regularization have a minor effect on the reconstruction quality of deeper layer; in fact, a strong regularization occasionally results in a *smaller* reconstruction error. At the same time, we noted that regularization can significantly improve the interpretability of the reconstructions for such layers.

In the rest of the section, visualizations are generated trading-off quantitative fidelity and interpretability. For AlexNet and VGG-M, we choose $C = 300$ up to relu3, $C = 100$ up to relu4, $C = 20$ up to relu5, and $C = 1$ for

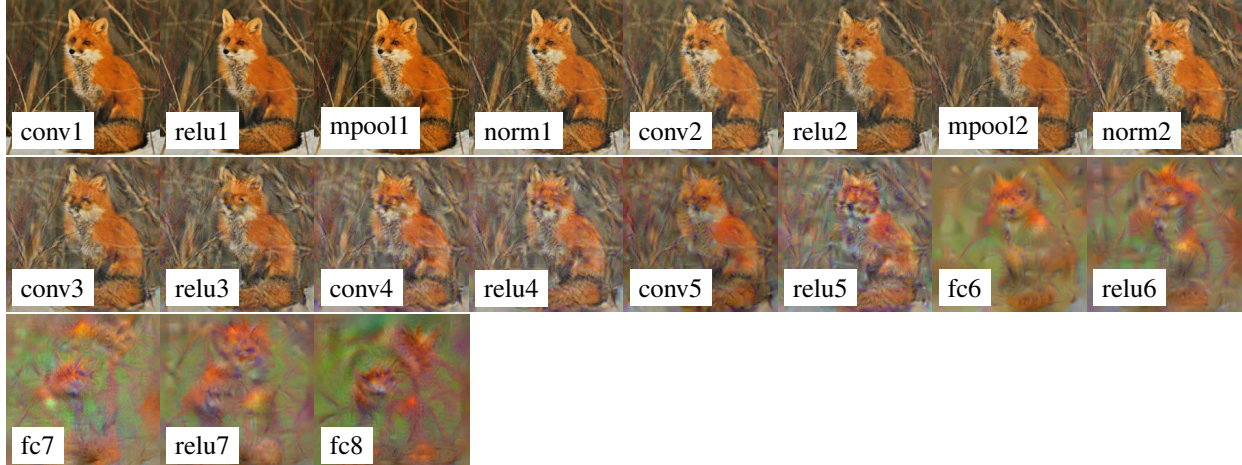


Figure 5: AlexNet inversions (all layers) from the representation of the “red fox” image obtained from each layer of AlexNet.

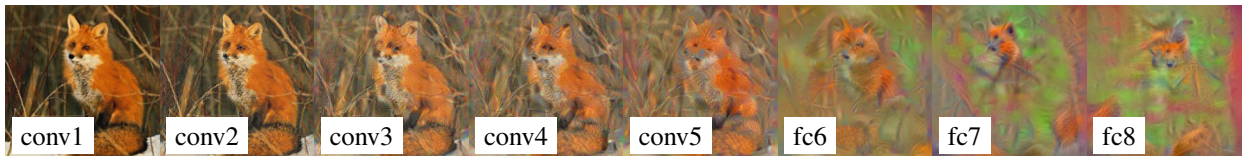


Figure 6: VGG-M inversions (selected layers). This figure is best viewed in color.

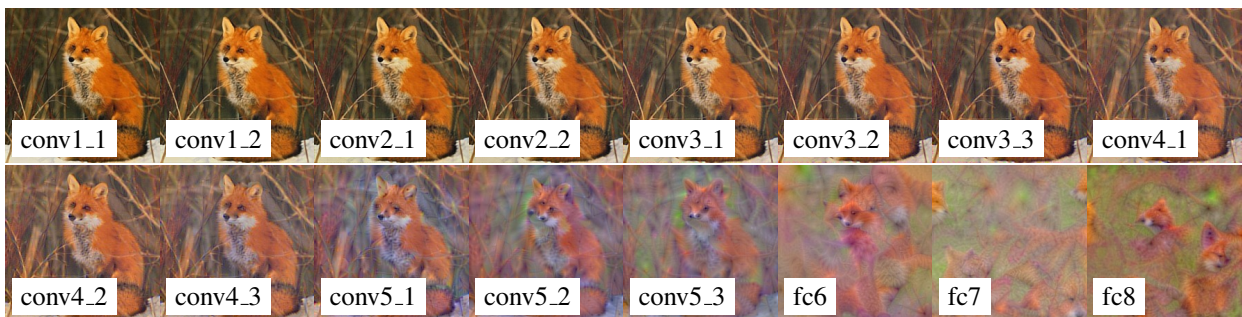


Figure 7: VGG-VD-16 inversions (selected layers). This figure is best viewed in color.

C	1	2	3	4	5	6	7	8	9	10	11	12	13	14	15	16	17	18	19	20
	conv1	relu1	norm1	pool1	conv2	relu2	norm2	pool2	conv3	relu3	conv4	relu4	conv5	relu5	pool5	fc6	relu6	fc7	relu7	fc8
1	69.5 ± 10.3	69.0 ± 10.6	61.4 ± 8.1	59.2 ± 7.7	57.0 ± 8.5	52.0 ± 6.8	50.4 ± 6.4	45.6 ± 5.7	37.3 ± 4.9	39.1 ± 5.2	32.2 ± 4.3	34.5 ± 4.6	24.9 ± 3.5	29.0 ± 4.2	26.4 ± 4.0	19.0 ± 2.5	24.6 ± 4.0	18.5 ± 3.5	21.4 ± 3.9	13.6 ± 2.9
20	35.3 ± 7.6	34.9 ± 7.9	32.6 ± 6.1	28.5 ± 4.9	22.7 ± 4.3	23.0 ± 4.7	23.3 ± 4.9	20.4 ± 4.0	16.5 ± 3.1	17.5 ± 3.3	15.0 ± 2.5	16.6 ± 2.8	12.1 ± 1.8	17.3 ± 3.1	16.3 ± 3.4	12.4 ± 1.8	19.4 ± 4.2	15.1 ± 3.0	17.0 ± 2.4	11.3 ± 2.0
100	21.1 ± 5.9	20.9 ± 6.2	19.9 ± 5.0	18.6 ± 5.0	13.2 ± 3.6	14.4 ± 3.0	14.9 ± 3.9	13.0 ± 4.2	11.3 ± 3.4	12.9 ± 2.7	11.6 ± 3.3	13.7 ± 2.7	9.6 ± 3.5	16.6 ± 1.9	16.3 ± 4.1	11.3 ± 4.5	19.7 ± 5.3	13.7 ± 2.6	15.6 ± 3.3	9.6 ± 2.1
300	14.2 ± 5.0	14.1 ± 5.3	13.6 ± 4.5	14.5 ± 2.9	9.6 ± 3.5	11.1 ± 3.8	11.6 ± 3.4	10.6 ± 3.4	9.9 ± 2.9	12.0 ± 4.0	11.0 ± 3.4	13.4 ± 4.4	9.0 ± 2.1	17.3 ± 5.2	17.5 ± 5.6	11.2 ± 2.1	20.2 ± 6.1	12.9 ± 2.6	14.9 ± 3.5	9.0 ± 2.0

Table 5: Average feature reconstruction errors obtained for each layer of AlexNet and different data fidelity term weights C .

the remaining layers. For VGG-VD we use $C = 300$ up to conv4_3, $C = 100$ for conv5_1, $C = 20$ up to conv5_3, and $C = 1$ onwards.

5.2.2 Inversion of different layers

Next, we study qualitatively the reconstructions obtained from different layers of the three CNNs for a test image (“red fox”). In particular, Figure 5 shows the reconstructions obtained from each layer of AlexNet and Figure 6 and Figure 7 do the same for all the linear (convolutional and fully connected) layers of VGG-M and VGG-VD.

The progression is remarkable. The first few layers of all the networks compute a code of the image that is nearly exactly invertible. All the layers prior to the fully-connected ones preserve instance-specific details of the image, although with increasing fuzziness. The 4,096-dimensional fully connected layers discard more geometric as well as instance-specific information as they invert back to a *composition of parts similar but not identical to the ones found in the original image*. Unexpectedly, even the very last layer, fc8, whose 1,000 components are in principle category predictors, still appears to preserve instance-specific details of the image.

Comparing different architectures, VGG-M reconstructions are sharper and more detailed than the ones obtained from AlexNet, as it may be expected due to the denser and higher dimensional filters used here (compare for example conv4 in Figure 5 and Figure 6). VGG-VD emphasizes these differences more. First, abstractions are achieved much more gradually in this architecture. For example, conv5_1, conv5_2 and conv5_3 reconstructions resemble the reconstructions from conv5 in AlexNet and VGG-M, despite the fact that there are three times more intermedi-

ate layers in VGG-VD. Nevertheless, fine details are preserved more accurately in the deep layers in this architecture (compare for example the nose and eyes of the fox in conv5 in VGG-M and conv5_1 – conv5_3 in VGG-VD).

Another difference we noted here, as well as in Figure 13 is that reconstructions from deep VGG-VD layers are often more zoomed-in compared to other networks (see for example the “abstract art” and “monkey” reconstructions from fc7 in Figure 8). The preference of VGG-VD for large, detailed object occurrences may be explained by its better ability to represent fine-grained object details, such as textures.

5.2.3 Reconstruction ambiguity and invariances

Next, Figure 8 examines the invariances captured by the VGG-VD codes by comparing multiple reconstructions obtained from several deep layers. A careful examination of these images reveals that the codes capture progressively larger deformations of the object. In the “flamingo” image, for example, conv5_2 reconstructions show slightly different body poses, evident from the different leg configurations. In the “abstract art” test image, a close examination of the reconstructions reveals that, while the texture is preserved well, the instance-specific details of the geometric pattern are in fact completely different. This case is also remarkable as the training data for VGG-VD, i.e. ImageNet ILSVRC, does not contain any such pattern suggesting that these codes are indeed rather generic. Inversions from fc7 result in multiple copies of the object/parts at different positions and scales for the “flamingo” and “monkey” cases. For the “monkey” and “abstract art” case, inversions appear to result in a magnified version of the pattern. The preference for reconstruct-

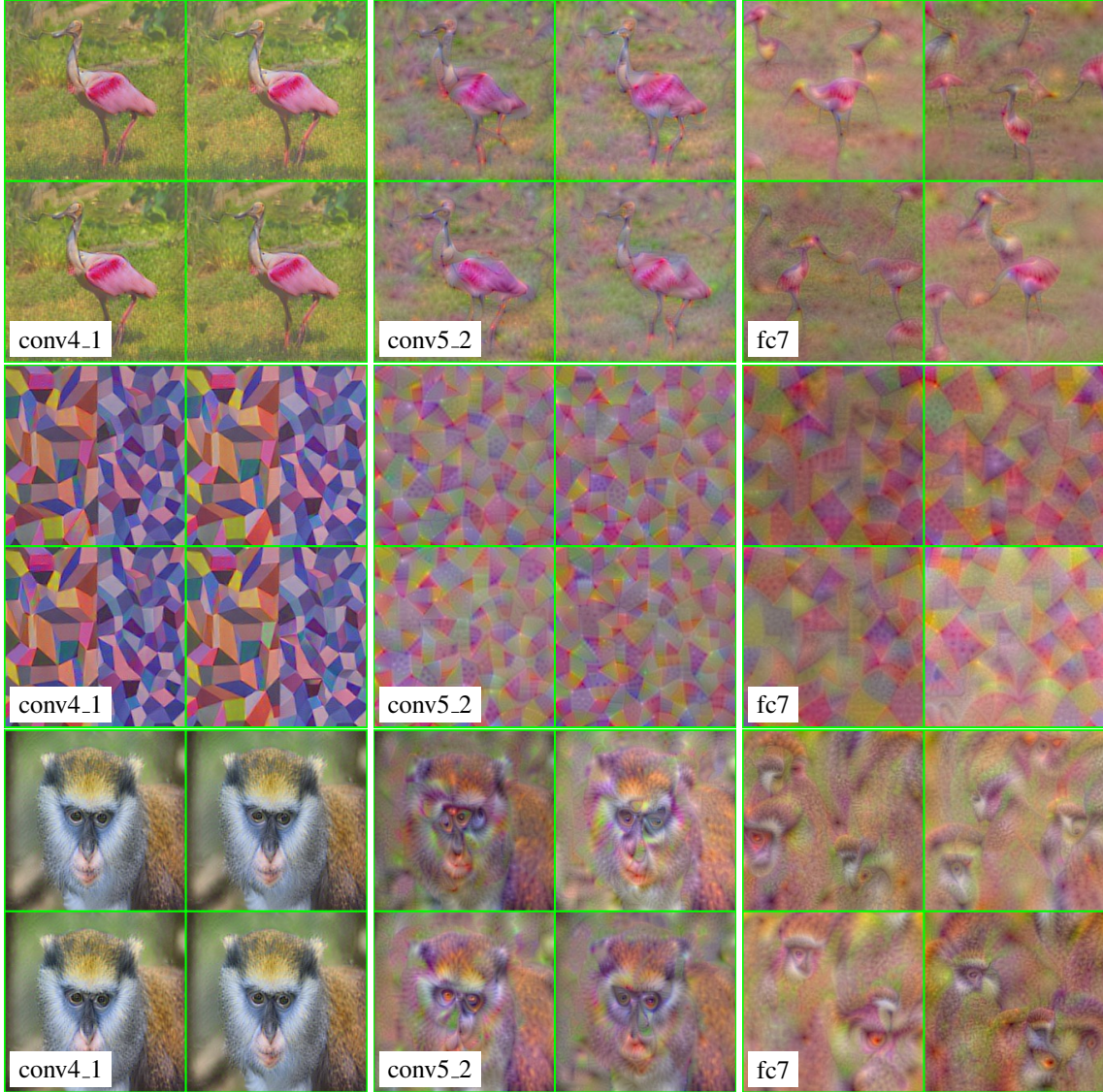


Figure 8: For three test images, “flamingo”, “abstract art”, and “monkey”, we generate four different reconstructions from layers conv4_1 , conv5_2 , and fc7 in VGG-VD. This figure is best seen in color.

ing larger object scales seem to be typical of VGG-VD (see also Figure 13).

Note that all these reconstructions and the original images are nearly indistinguishable from the viewpoint of the CNN representation; we conclude in particular that

the deepest layers find the the original images and a number of scrambled parts equivalent. This may be consider another type of natural confounders for CNNs alternative to [29].

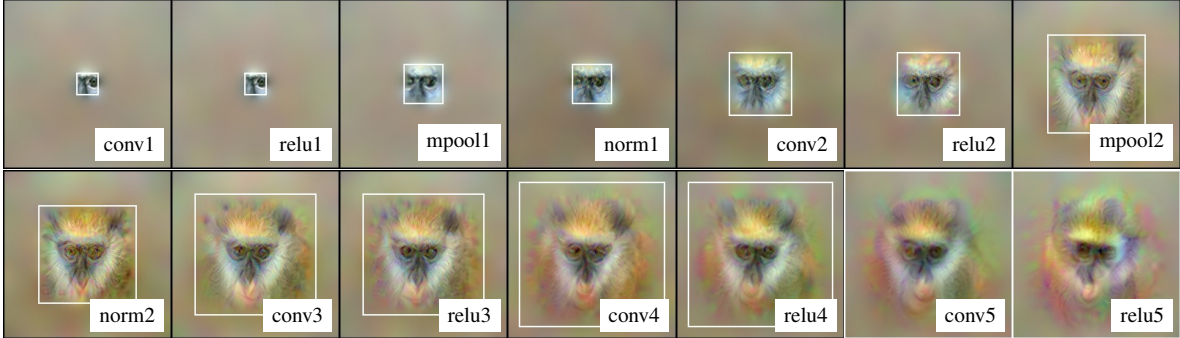


Figure 9: Reconstructions of the “monkey” image from a central 5×5 window of feature responses in the convolutional layers of CaffeRef. The white box marks the overall receptive field of the 5×5 window.

5.2.4 Reconstruction biases

It is interesting to note that many of the inverted images have large green regions. This property is likely to be intrinsic to the networks and not induced, for example, by the choice of natural image prior, the effect of which is demonstrated in Figure 2-3.2.3. The prior only encourages smoothness as it is equivalent (for $\beta = 2$) to penalizing high-frequency components of the reconstructed image. Importantly, the prior is applied to all color channels equally. When gradually removing the prior, random high-frequency components dominate and it is harder to discern a human-interpretable signal. The green color, however, persists; we verified this on several example images as well as different networks, including the MIT Places CNN [50] which is not trained on ImageNet. This may be analogous to the fact that the human retina is also more sensitive to the green color band.

5.2.5 Inversion from selected representation components

We now examine reconstructions obtained from subset of neural responses in different CNN layers. Figure 9 explores the *locality* of the codes by reconstructing a central 5×5 patch of features in each layer. The regularizer encourages portions of the image that do not contribute to the neural responses to be switched off. The locality of the features is obvious in the figure; what is less obvious is that the effective receptive field of the neurons is in some cases significantly smaller than the theoretical one

shown as a white box in the image.

Finally, Figure 10 reconstructs images from two different subsets of feature channels for CaffeRef. These subsets are induced by the fact that the first several layers (up to norm2) of the CaffeRef architecture are trained to have blocks of independent filters [20]. Reconstructing from each subset individually clearly shows that one group is tuned towards color information whereas the second one is tuned towards sharper edges and luminance components. Remarkably, this behavior emerges spontaneously in the learned network.

6 Visualizing CNNs using activation maximization

In this section we apply the activation maximization method to the study of deep CNNs. The inner-product loss Equation 4 is used in the objective (1), and the reference vector Φ_0 is set to the one-hot indicator vector of the representation component that we would like to visualize. It was not possible to find a constant setting for the normalization factor Z in Equation 4 that would work well for all architectures and features; instead Z is set to the following value:

$$Z = \frac{1}{M\rho^2}$$

where M is the maximum value achieved by the representation component in the ImageNet ILSVRC 2012 validation data and ρ the size of the component receptive field,

as reported in Table 1. As in 5.2 the jitter amount T in (section 3.2.3) is set to a fourth of the stride of the feature (Table 1-2-3) and all the other parameters are set as described in section 3.3 (including $C = 1$).

Figure 11 shows the visual patterns obtained by maximally activating the few components in the convolutional layers of VGG-M. Similarly to [49] and [47], the complexity of the patterns increases substantially with depth. The first convolutional layer conv1 captures colored edges and blobs, but the complexity of the patterns generated by conv3, conv4 and conv5 is remarkable. While some of these pattern do evoke objects or objects parts, it remains difficult to associate to them a clear semantic interpretation (differently from [47] we prefer to avoid hand-picking semantically interpretable filters). This is not entirely surprising given that the representation is distributed and activations may need to be combined to form a meaning. Experiments from AlexNet yielded entirely analogous if a little blurrier results.

Figure 12 shows the patterns obtained from VGG-VD. The complexity of the patterns builds up more gradually than for VGG-M and AlexNet. Qualitatively, the complexity of the stimuli in conv5 in AlexNet and VGG-M seems to be comparable to conv4_3 and conv5_1 in VGG-VD. conv5_2 and conv5_3 do appear to be significantly more complex, however. A second observation is that the reconstructed colors tend to be much more saturated, probably due to the lack of normalization layers in the architecture. Thirdly, we note that reconstructions contain significantly more fine-grained details, and in particular tiny blob-like structures, which probably activate very strongly the first very small filters in the network.

Figure 13 repeats the experiment from [35], more recently reprised by [47] and [28], and maximizes the component of fc8 that corresponds to a given class prediction. Four classes are considered: two similar animals (“black swan” and “goose”), a different one (“tree frog”), and an inanimate object (“cheeseburger”). We note that in all cases it is easy to identify several parts or even instance of the target object class. However, reconstructions are fragmented and scrambled, indicating that the representations are highly invariant to occlusions and pose changes. Secondly, reconstructions from VGG-M are considerably sharper than the ones obtained from AlexNet, as could be expected. Thirdly, VGG-VD-16 differs significantly from the other two architectures. Colors are more “washed

out”, which we impute to the lack of normalization in the architecture as for Figure 12. Reconstructions tends to focus on much larger objects; for example, the network clearly captures the feather pattern of the bird as well as the rough skin of the frog.

7 Visualizing CNNs using caricaturization

Our last visualization is inspired by Google’s Inceptionism [28]. It is similar to activation maximization (section 6) and uses in fact the same formulation for Equation 1 with the inner-product loss Equation 4. However, there are two key differences. First, the target mask is now set to

$$\Phi_0 = \max\{0, \Phi(\mathbf{x}_0)\}$$

where \mathbf{x}_0 is a reference image and the normalization factor Z is set to $1/\|\Phi_0\|$. Second, the optimization is started from the image \mathbf{x}_0 itself.

The idea of this visualization is to exaggerate any pattern in \mathbf{x}_0 that is active in the representation $\Phi(\mathbf{x}_0)$, hence creating a “caricature” of the image according to this model. Furthermore, differently from activation maximization, this visualization works with combinations of multiple activations instead of individual ones.

Figure 14 shows the caricatures of the “red-fox” image obtained from the different layers of VGG-M. Applied to the first block of layers, the procedure simply saturates the color. conv2 appears to be tuned to long, linear structures, conv4 to round ones, and conv5 to the head of the fox (part). The fully connected layers generate mixtures of fox heads, including hallucinating several in the background, as already noted in [28]. Figure 15 shows the caricatures obtained from selected layers of VGG-M and VGG-VD, with similar results.

8 Summary

There is a growing interest in methods that can help us understanding computer vision representations, and in particular representations learned automatically from data such as deep CNNs. Recently, several authors have proposed complementary visualization techniques to do so.

In this manuscript we have extended our previous work on inverting representations using natural pre-images to a unified framework that encompasses several visualization types. We have then experimented with three such visualizations, inversion, activation maximization, and caricaturization, and used those to probe and compare standard classic representations and CNNs.

The robustness of our visualization method has been assessed quantitatively in the case of the inversion problem by comparing the output of our approach to earlier feature inversion techniques. The most important results, however, emerged from an analysis of the visualizations obtained from deep CNNs; some of these are: the fact that photometrically accurate information is preserved deep down in CNNs, that even very deep layers contain instance-specific information about objects, that intermediate convolutional layers capture local invariances to pose and fully connected layer to large variations in the object layouts, that individual CNN components code for complex but, for the most part, not semantically-obvious patterns, and that different CNN layers appear to capture different types of structures in images, from lines and curves to parts.

We believe that these visualization methods can be used as direct diagnostic tools in further research in CNNs. For example, an interesting problem is to look for semantically-meaningful activation patterns in deep CNN layers (given that individual responses are often not semantic); inversion, or variants of activation maximization, can be used to validate such activation patterns by means of visualizations.

Acknowledgements

We gratefully acknowledge the support of the ERC StG IDIUI for Andrea Vedaldi and of BP for Aravindh Mahendran.

References

- [1] Bishop, C.M.: *Neural Networks for Pattern Recognition*. Clarendon Press, Oxford (1995)
- [2] Chatfield, K., Simonyan, K., Vedaldi, A., Zisserman, A.: Return of the devil in the details: Delving deep into convolutional nets. In: Proc. BMVC (2014)
- [3] Chen, Y., Ranftl, R., Pock, T.: A bi-level view of inpainting-based image compression. In: Proc. of Computer Vision Winter Workshop (2014)
- [4] Csurka, G., Dance, C.R., Dan, L., Willamowski, J., Bray, C.: Visual categorization with bags of keypoints. In: Proc. ECCV Workshop on Stat. Learn. in Comp. Vision (2004)
- [5] Dalal, N., Triggs, B.: Histograms of oriented gradients for human detection. In: CVPR (2005)
- [6] d'Angelo, E., Alahi, A., Vandergheynst, P.: Beyond bits: Reconstructing images from local binary descriptors. In: ICPR, pp. 935–938 (2012)
- [7] Dosovitskiy, A., Brox, T.: Inverting convolutional networks with convolutional networks. CoRR (abs/1506.02753) (2015)
- [8] Duchi, J., Hazan, E., Singer, Y.: Adaptive subgradient methods for online learning and stochastic optimization. Journal of Machine Learning Research **12** (2011)
- [9] Erhan, D., Bengio, Y., Courville, A., Vincent, P.: Visualizing higher-layer features of a deep network. Tech. Rep. 1341, University of Montreal (2009)
- [10] Felzenszwalb, P.F., Girshick, R.B., McAllester, D., Ramanan, D.: Object detection with discriminatively trained part based models. IEEE Transactions on Pattern Analysis and Machine Intelligence **32**(9), 1627–1645 (2010)
- [11] Gatys, L.A., Ecker, A.S., Bethge, M.: A neural algorithm of artistic style. CoRR (2015)
- [12] Gatys, L.A., Ecker, A.S., Bethge, M.: Texture synthesis and the controlled generation of natural stimuli using convolutional neural networks. In: Proc. NIPS (2015)
- [13] Girshick, R.B., Felzenszwalb, P.F., McAllester, D.: Discriminatively trained deformable part models, release 5. <http://people.cs.uchicago.edu/~rbg/latent-release5/>

[14] Hinton, G.E., Salakhutdinov, R.R.: Reducing the dimensionality of data with neural networks. *Science* **313**(5786) (2006)

[15] Jégou, H., Douze, M., Schmid, C., Pérez, P.: Aggregating local descriptors into a compact image representation. In: *CVPR* (2010)

[16] Jensen, C.A., Reed, R.D., Marks, R.J., El-Sharkawi, M., Jung, J.B., Miyamoto, R., Anderson, G., Eggen, C.: Inversion of feedforward neural networks: algorithms and applications. *Proc. of the IEEE* **87**(9) (1999)

[17] Jia, Y.: Caffe: An open source convolutional architecture for fast feature embedding. <http://caffe.berkeleyvision.org/> (2013)

[18] Kato, H., Harada, T.: Image reconstruction from bag-of-visual-words. In: *CVPR* (2014)

[19] Krishnan, D., Fergus, R.: Fast image deconvolution using hyper-laplacian priors. In: *NIPS* (2009)

[20] Krizhevsky, A., Sutskever, I., Hinton, G.E.: Imagenet classification with deep convolutional neural networks. In: *NIPS* (2012)

[21] Lee, S., Kil, R.M.: Inverse mapping of continuous functions using local and global information. *IEEE Trans. on Neural Networks* **5**(3) (1994)

[22] Leung, T., Malik, J.: Representing and recognizing the visual appearance of materials using three-dimensional textons. *IJCV* **43**(1) (2001)

[23] Linden, A., Kindermann, J.: Inversion of multilayer nets. In: *Proc. Int. Conf. on Neural Networks* (1989)

[24] Lowe, D.G.: Object recognition from local scale-invariant features. In: *ICCV* (1999)

[25] Lowe, D.G.: Distinctive image features from scale-invariant keypoints. *IJCV* **2**(60), 91–110 (2004)

[26] Lu, B.L., Kita, H., Nishikawa, Y.: Inverting feed-forward neural networks using linear and nonlinear programming. *IEEE Trans. on Neural Networks* **10**(6) (1999)

[27] Mahendran, A., Vedaldi, A.: Understanding deep image representations by inverting them. In: *Proc. CVPR* (2015)

[28] Mordvintsev, A., Olah, C., Tyka, M.: Inceptionism: Going deeper into neural networks (2015). URL <http://googleresearch.blogspot.co.uk/2015/06/inceptionism-going-deeper-into-neural.html>

[29] Nguyen, A., Yosinski, J., Clune, J.: Deep neural networks are easily fooled: High confidence predictions for unrecognizable images. In: *Proc. CVPR* (2015)

[30] Nowak, E., Jurie, F., Triggs, B.: Sampling strategies for bag-of-features image classification. In: *ECCV* (2006)

[31] Perronnin, F., Dance, C.: Fisher kernels on visual vocabularies for image categorization. In: *CVPR* (2006)

[32] Portilla, J., Simoncelli, E.P.: A parametric texture model based on joint statistics of complex wavelet coefficients. *IJCV* (2000)

[33] Russakovsky, O., Deng, J., Su, H., Krause, J., Satheesh, S., Ma, S., Huang, Z., Karpathy, A., Khosla, A., Bernstein, M.S., Berg, A.C., Fei-Fei, L.: Imagenet large scale visual recognition challenge. *CoRR* **abs/1409.0575** (2014). URL <http://arxiv.org/abs/1409.0575>

[34] Sermanet, P., Eigen, D., Zhang, X., Mathieu, M., Fergus, R., LeCun, Y.: Overfeat: Integrated recognition, localization and detection using convolutional networks. In: *CoRR*, vol. *abs/1312.6229* (2014)

[35] Simonyan, K., Vedaldi, A., Zisserman, A.: Deep inside convolutional networks: Visualising image classification models and saliency maps. In: *Proc. ICLR* (2014)

[36] Sivic, J., Zisserman, A.: Video Google: A text retrieval approach to object matching in videos. In: *ICCV* (2003)

- [37] Szegedy, C., Zaremba, W., Sutskever, I., Bruna, J., Erhan, D., Goodfellow, I.J., Fergus, R.: Intriguing properties of neural networks. *CoRR* **abs/1312.6199** (2013)
- [38] Tatu, A., Lauze, F., Nielsen, M., Kimia, B.: Exploring the representation capabilities of the HOG descriptor. In: *ICCV Workshop* (2011)
- [39] Várkonyi-Kóczy, A.R., Rövid, A.: Observer based iterative neural network model inversion. In: *IEEE Int. Conf. on Fuzzy Systems* (2005)
- [40] Vedaldi, A.: An open implementation of the SIFT detector and descriptor. *Tech. Rep. 070012, UCLA CSD* (2007)
- [41] Vedaldi, A., Lenc, K.: MatConvNet: CNNs for MATLAB. <http://www.vlfeat.org/matconvnet/> (2014)
- [42] Vondrick, C., Khosla, A., Malisiewicz, T., Torralba, A.: HOGgles: Visualizing object detection features. In: *ICCV* (2013)
- [43] Wang, J., Yang, J., Yu, K., Lv, F., Huang, T., Gong, Y.: Locality-constrained linear coding for image classification. In: *CVPR* (2010)
- [44] Weinzaepfel, P., Jégou, H., Pérez, P.: Reconstructing an image from its local descriptors. In: *CVPR* (2011)
- [45] Williams, R.J.: Inverting a connectionist network mapping by back-propagation of error. In: *Proc. CogSci* (1986)
- [46] Yang, J., Yu, K., Huang, T.: Supervised translation-invariant sparse coding. In: *CVPR* (2010)
- [47] Yosinski, J., Clune, J., Nguyen, A., Fuchs, T., Lipson, H.: Understanding neural networks through deep visualization. In: *Proc. ICML Workshop* (2015)
- [48] Zeiler, M.D.: ADADELTA: An adaptive learning rate method. *CoRR* (arXiv:1212.5701) (2012)
- [49] Zeiler, M.D., Fergus, R.: Visualizing and understanding convolutional networks. In: *ECCV* (2014)
- [50] Zhou, B., Lapedriza, A., Xiao, J., Torralba, A., Oliva, A.: Learning deep features for scene recognition using places database. In: *NIPS*, pp. 487–495 (2014)
- [51] Zhou, X., Yu, K., Zhang, T., Huang, T.S.: Image classification using super-vector coding of local image descriptors. In: *ECCV* (2010)

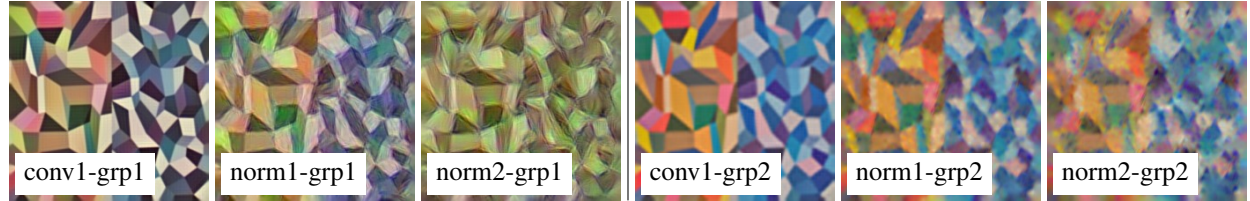


Figure 10: **CNN neural streams.** Reconstructions of the “abstract” test image from either of the two neural streams in CaffeRef. This figure is best seen in color.

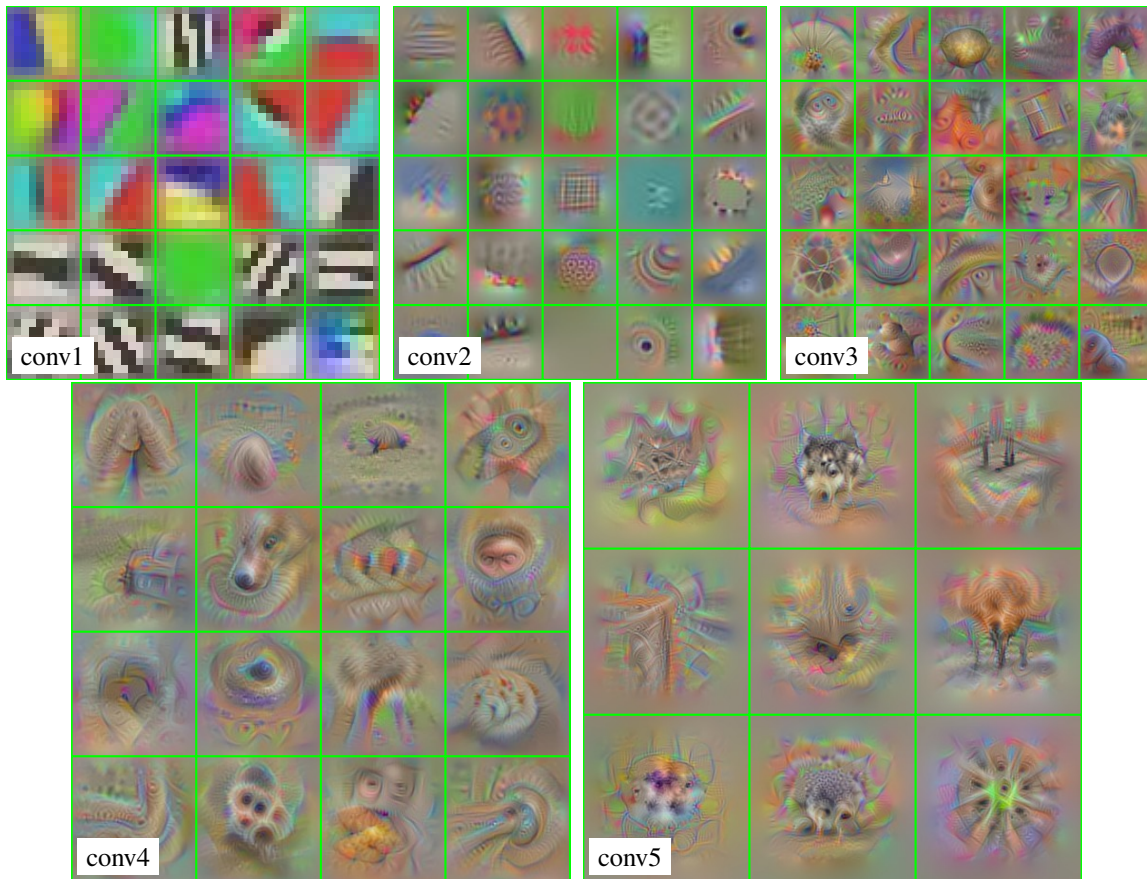


Figure 11: Activation maximization of the first filters of each convolutional layer in VGG-M.

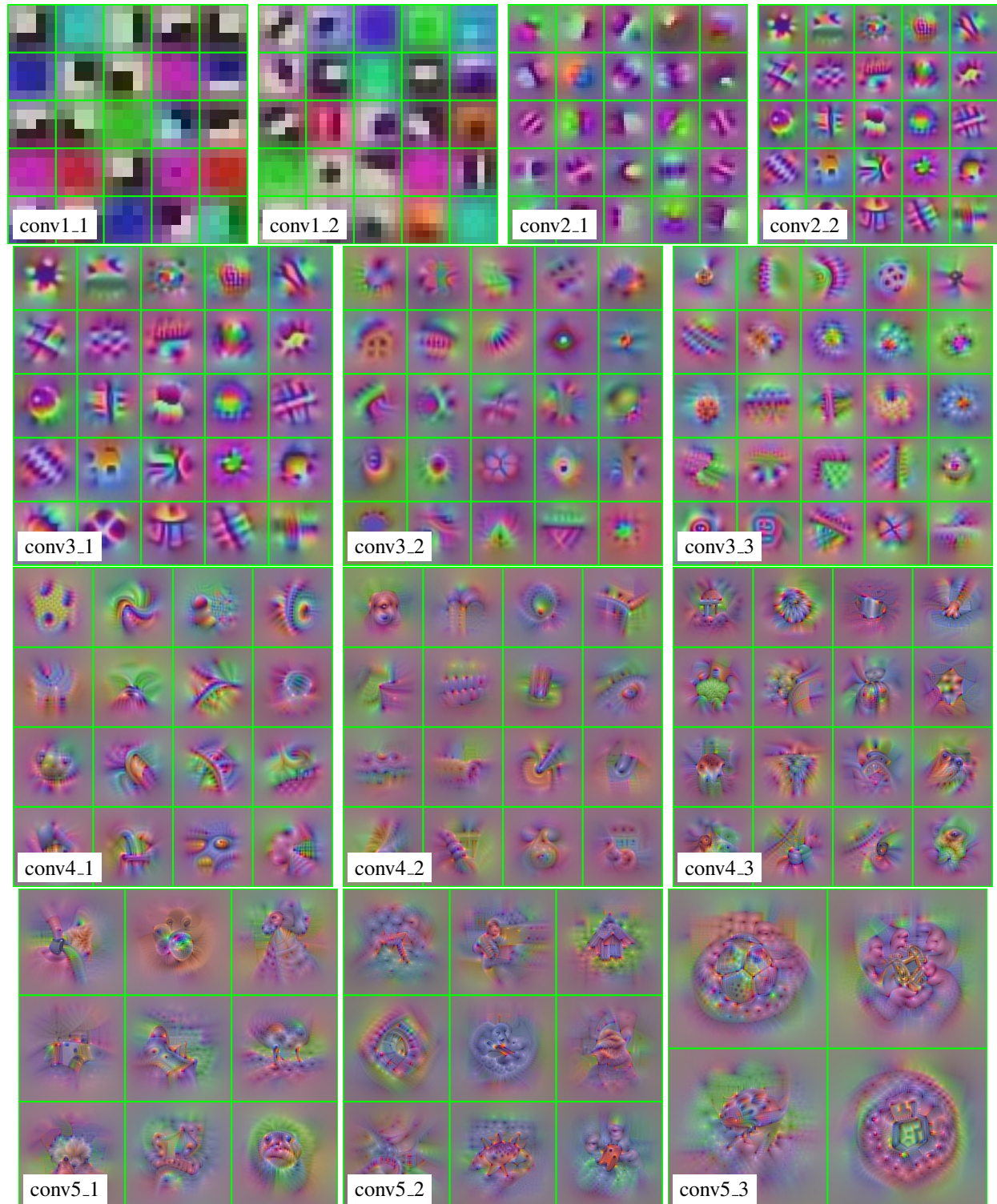


Figure 12: Activation maximization of the first filters for each convolutional layer in VGG-VD-16. ²²

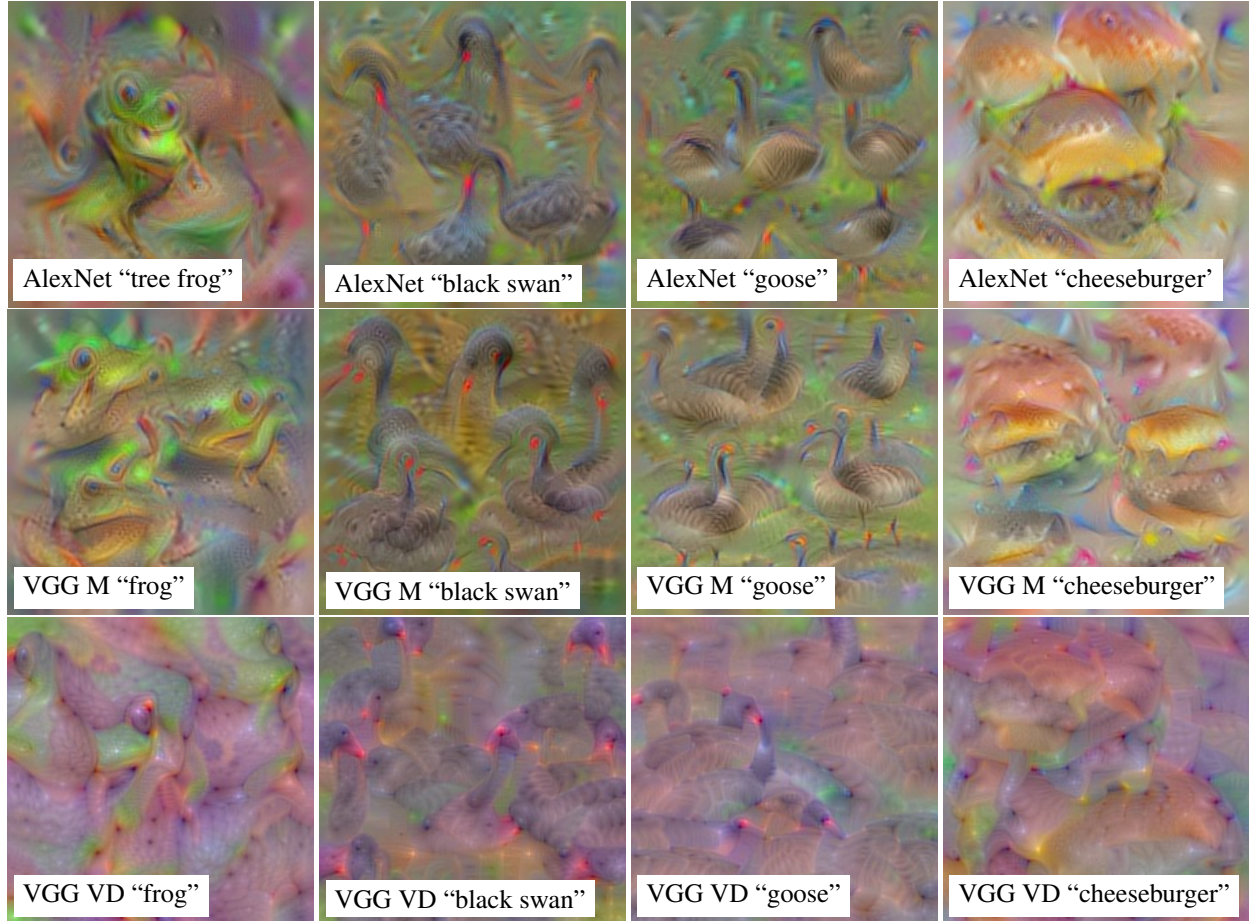


Figure 13: Activation maximization for the second to last layer of AlexNet, VGG-M, VGG-VD-16 for the classes “frog”, “black swan”, “goose”, and “vending machine”. The second to last layer codes directly for different classes, before softmax normalization.

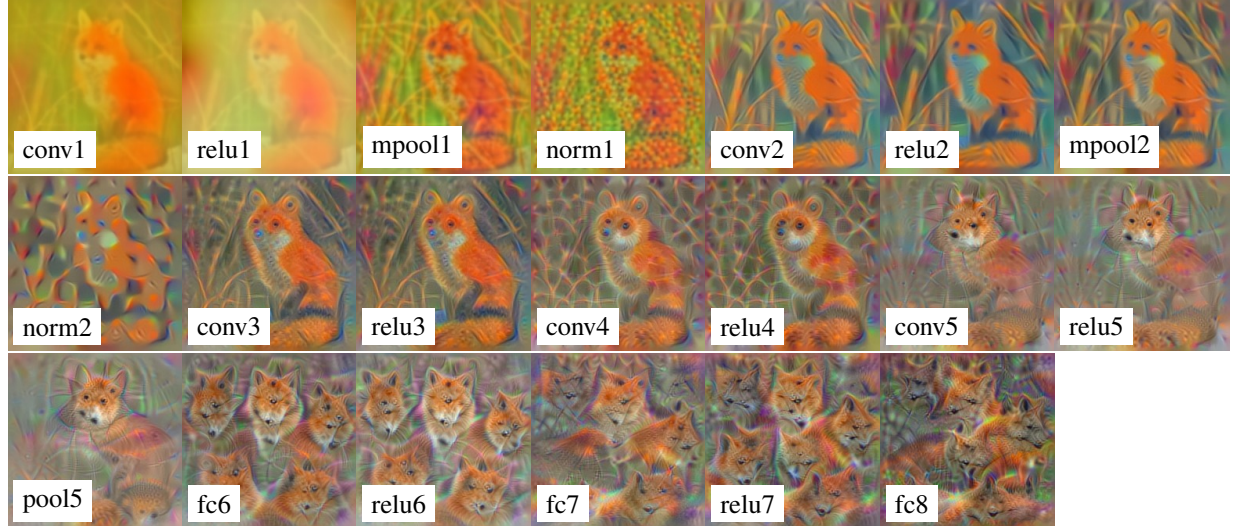


Figure 14: Caricatures of the “red fox” image obtained from the different layers in VGG-M.

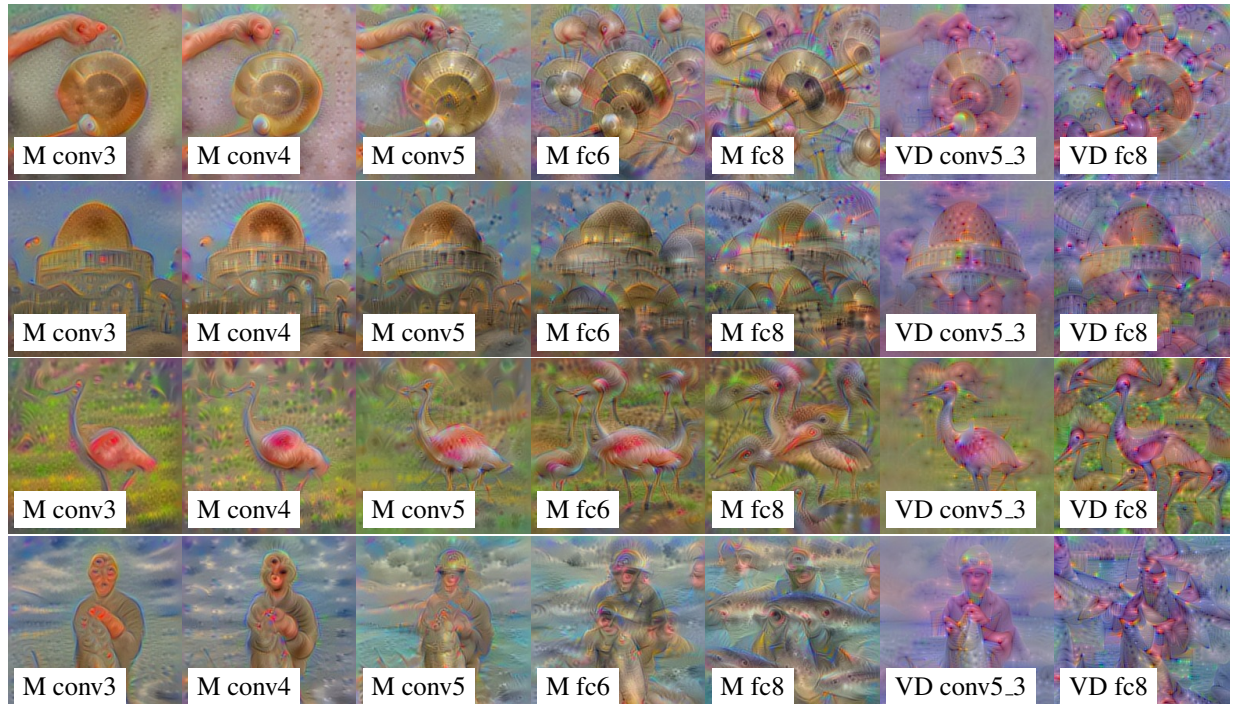


Figure 15: Caricatures of a number of test images obtained from the different layers of VGG-M (conv3, conv4, conv5, fc6, fc8) and VGG-VD (conv5_3 and fc8).